

ARMY RESEARCH LABORATORY



Validation Testing and Numerical Modeling of Advanced Armor Materials

by Stephan R. Bilyk and Thomas A. Bjerke

ARL-TR-6244

November 2012

NOTICES

Disclaimers

The findings in this report are not to be construed as an official Department of the Army position unless so designated by other authorized documents.

Citation of manufacturer's or trade names does not constitute an official endorsement or approval of the use thereof.

Destroy this report when it is no longer needed. Do not return it to the originator.

Army Research Laboratory

Aberdeen Proving Ground, MD 21005-5069

ARL-TR-6244

November 2012

Validation Testing and Numerical Modeling of Advanced Armor Materials

Stephan R. Bilyk
Weapons and Materials Research Directorate, ARL

Thomas A. Bjerke
University of Maryland, Department of Mechanical Engineering

REPORT DOCUMENTATION PAGE				Form Approved OMB No. 0704-0188	
Public reporting burden for this collection of information is estimated to average 1 hour per response, including the time for reviewing instructions, searching existing data sources, gathering and maintaining the data needed, and completing and reviewing the collection information. Send comments regarding this burden estimate or any other aspect of this collection of information, including suggestions for reducing the burden, to Department of Defense, Washington Headquarters Services, Directorate for Information Operations and Reports (0704-0188), 1215 Jefferson Davis Highway, Suite 1204, Arlington, VA 22202-4302. Respondents should be aware that notwithstanding any other provision of law, no person shall be subject to any penalty for failing to comply with a collection of information if it does not display a currently valid OMB control number. PLEASE DO NOT RETURN YOUR FORM TO THE ABOVE ADDRESS.					
1. REPORT DATE (DD-MM-YYYY) November 2012	2. REPORT TYPE Final	3. DATES COVERED (From - To) September 10, 2012			
4. TITLE AND SUBTITLE Validation Testing and Numerical Modeling of Advanced Armor Materials			5a. CONTRACT NUMBER		
			5b. GRANT NUMBER		
			5c. PROGRAM ELEMENT NUMBER		
6. AUTHOR(S) Stephan R. Bilyk and Thomas A. Bjerke*			5d. PROJECT NUMBER		
			5e. TASK NUMBER		
			5f. WORK UNIT NUMBER		
7. PERFORMING ORGANIZATION NAME(S) AND ADDRESS(ES) U.S. Army Research Laboratory ATTN: RDRL-WMP-C Aberdeen Proving Ground, MD 21005-5069			8. PERFORMING ORGANIZATION REPORT NUMBER ARL-TR-6244		
9. SPONSORING/MONITORING AGENCY NAME(S) AND ADDRESS(ES)			10. SPONSOR/MONITOR'S ACRONYM(S)		
			11. SPONSOR/MONITOR'S REPORT NUMBER(S)		
12. DISTRIBUTION/AVAILABILITY STATEMENT Approved for public release; distribution is unlimited.					
13. SUPPLEMENTARY NOTES *University of Maryland, Department of Mechanical Engineering					
14. ABSTRACT This report documents a preliminary experimental, analytical, and modeling effort for validating a numerical approach using constitutive material strength response with an appropriate yield surface model. The research is sub-divided into three areas: engineering design and specimen preparation for Taylor impact testing, analytical solution for the dynamic yield strength of the materials used, and numerical modeling of the Taylor impact test for validation of a simplified constitutive response model. The material of interest is called metal matrix composite (MMC) and consist of a strengthening component embedded in an aluminum alloy matrix. For this study, we perform Taylor impact tests on a unique, lightweight aluminum-based MMC. We compare the observed deformation with results obtained from companion experiments using specimens made from 6061-T6 aluminum alloy only. We perform a detailed analysis of the deformed specimen shapes to determine the dynamic yield strength. Additionally, hydrocode simulations of the Taylor impact test using material models appropriate for the specimen material types are performed and compared to experimental data for model validation. This work provides the foundation for developing and validating robust MMC material models that may ultimately lead to innovative lightweight armor concepts.					
15. SUBJECT TERMS Taylor impact, metal matrix composite, Gurson model					
16. SECURITY CLASSIFICATION OF:			17. LIMITATION OF ABSTRACT UU	18. NUMBER OF PAGES 40	19a. NAME OF RESPONSIBLE PERSON Stephen R. Bilyk
a. REPORT Unclassified	b. ABSTRACT Unclassified	c. THIS PAGE Unclassified			19b. TELEPHONE NUMBER (Include area code) 410-278-2976

Standard Form 298 (Rev. 8/98)
Prescribed by ANSI Std. Z39.18

Contents

List of Figures	iv
List of Tables	v
Acknowledgments	vi
1. Introduction	1
2. Experimental Methods	2
2.1 Materials, Equipment, and Procedures.....	3
2.1.1 Projectiles	3
2.1.2 Rigid Anvil	6
2.1.3 Instrumentation, Experimental Setup and Procedures	7
3. Analytical Consideration	9
4. Numerical Simulations	11
5. Results	15
6. Summary and Conclusions	23
7. References	24
Appendix. MTS Model Parameters for 6061-T6 Aluminum	29
List of Symbols, Abbreviations, and Acronyms	30
Distribution List	31

List of Figures

Figure 1. Original schematic of a Taylor impact test (from reference 1).	3
Figure 2. Schematic of the metal matrix composite.	4
Figure 3. SEM images of (a) the ceramic MMC showing spherical cenospheres ranging between 30–50-microns diameter, (b) magnified view of an isolated cenosphere with an approximate diameter of 15 microns and 3–5 microns wall thickness.	5
Figure 4. Ceramic MMC plate, cut cylinders and elasto-foam launch sabots.	6
Figure 5. Schematic view of the assembly used for Taylor impact testing.	7
Figure 6. Photographic images of the Taylor impact test assembly including a view of the laser break screens.	8
Figure 7. Sabot stripping device, (a) side view, (b) top view, with bore reduction inserts and schematic.....	9
Figure 8. Schematic illustrating the reference configuration, initial conditions, boundary conditions and description of material response for the cenospheres MMC Taylor Impact Test. Note, the MMC material contained two distinct regions: (1) end-caps of aluminum only and (2) aluminum matrix with cenosphere inclusions. These regions were taken into account in the numerical modeling.	12
Figure 9. Observed results illustrating the dependence of final deformed length of the aluminum-ceramic cenosphere MMC to the original length.	17
Figure 10. Side profiles of the final deformed shapes for the MMC specimens from Taylor Impact tests using three different chamber pressures and specimen diameters.....	17
Figure 11. Observed results for MMC Taylor tests illustrating that final length deformed as a function of the density, strength, and impact velocity.	18
Figure 12. Comparison of plastic strain evolution using the von Mises (top) and Gurson yield surface (bottom) models for the aluminum matrix-ceramic cenosphere region with aluminum-only end-caps.....	19
Figure 13. Macroscopic sectioned view of deformed specimen and boxed regions for optical imaging.	20
Figure 14. MMC material microstructure of non-deformed region. Note the uniform spherical shapes of the inclusions; some spheres are not hollow and filled with aluminum and the dark regions are either sectioned inclusions or inclusions that were removed during sectioning/polishing.....	20
Figure 15. Micrograph of the MMC material in the mid-radial region (centerline) toward the impacted face. The low porosity region on the far left is the aluminum matrix-only end-cap. Note that the cenosphere profiles are changing from spherical on non-deformed right side to oval in the mid-region.	21
Figure 16. Micrograph of the MMC material in high strained corner area. The cenosphere near the end-cap/MMC interface are clearly collapsing during impact. The dark regions represent crushed pores/voids.	22

Figure 17. Evolution of porosity using the Gurson yield surface model for the aluminum matrix-ceramic cenosphere region. Note, the end-cap region was not shown in contour plot but was included in the numerical simulation.	23
--	----

List of Tables

Table 1. Experimental data and test results for impacts of aluminum matrix with cenospheres particles (metal matrix composite).....	16
Table 2. Comparison of predicted with observed results for 6061-T6 aluminum alloys (47) and the metal matrix composite.	18

Acknowledgments

We are indebted to invaluable computational and experimental technical advice provided by Dr. Richard C. Becker, PD. The authors would also like to thank Dr. Robert H. Carter, MMSD, for providing the MMC material and Dr. Clifford W. Hubbard, MMSD, for microscopy (SEM) operation. The experimental tests would not have been possible without the expertise provided by two outstanding technicians, William R. Edmanson and David E. MacKenzie. Additionally, we would like to thank Ronald S. Worthington for manufacturing the sabot stripper, and engineering technicians Jeffrey W. Ball, Robert W. Borys, and Colby T. Adams for immediately providing a high speed camera, camera assembly and operation.

1. Introduction

The process of improving vehicle ballistic protection relies on innovative armor concepts utilizing advanced, lightweight materials. Due to the complex processes present during a ballistic impact event, it is often difficult to identify the armor or material parameters that significantly influence performance. These controlling parameters can be identified by performing carefully instrumented impact experiments, examination of dominant parameters in analytical penetration mechanics solutions, or computational modeling of the ballistic impact event (1, 2). Once limiting performance parameters and defeat mechanisms are identified, the armor designer can seek to control these aspects for optimized and enhanced armor performance.

Paramount to modeling the performance of advanced armor materials during ballistic impact events has been the development and application of numerical algorithms called hydrocodes. After discretizing the penetrator and armor geometry into a fine computational domain or mesh, a hydrocode provides a spatial and temporal solution to the governing conservation equations of mass, momentum, and energy as applied to the ballistic boundary value problem. The success of accurately predicting armor performance is dependent on the ability to model the deformation and failure of the penetrator and armor materials during the impact and penetration process. Material behavior models, or constitutive relationships, are a mathematical representation of empirical and physically-based observations, typically from controlled experiments that probe the deformation behavior of a material at different deformation, or strain, rates (3–8).

Prior to use in hydrocodes for armor performance calculations, constitutive material models must be validated. The typical approach to validation involves comparison of model output with material response experiments, which span the strain rates relevant to a ballistic impact event. One such type of experiment, the Taylor impact test, was originally devised to determine the dynamic yield strength of materials at high strain rates. More recently, such tests have been used extensively to validate numerical codes for the simulation of plastic deformation (9–19). The test involves the impact of a flat-nosed cylindrical projectile on a hard/rigid anvil at normal incidence. The dimensions of the recovered specimens are measured and the deformed material is examined at the grain level for microstructural changes.

This research effort is focused on using the Taylor impact experiment for validation of a constitutive material model. The research is sub-divided into three areas: (1) engineering design and specimen preparation for Taylor impact testing, (2) analytical solution for the dynamic yield strength of the materials used, and (3) numerical modeling of the Taylor impact test for validation of a simplified constitutive response model. The material of interest is a metal matrix composite (MMC) consisting of a strengthening component embedded in an aluminum alloy matrix. MMC systems are of interest for light-weight armor materials suitable for vehicle and Soldier protection (20–24). MMC have shown some promise in providing improved multi-hit

capability over, for example, ceramic materials (25, 26) but this has not been verified with ballistic testing performed at the U.S. Army Research Laboratory (ARL). Conceptually, upon impact some amount of the penetrator's kinetic energy is absorbed by the collapsing hard particle inclusions. The shock velocity within the MMC is also altered. As the hard particles disrupt the threat and absorb energy, the propagation of cracks is limited by the relatively tough metal matrix. The ballistic performance of MMC materials can potentially be improved by coupling novel manufacturing processes to produce functionally graded MMC materials (27, 28).

For this study, we perform Taylor impact tests on a unique, lightweight aluminum-based MMC, which is a potential candidate material for underbody vehicle protection. We compare the observed deformation with results obtained from companion experiments using specimens made from the unreinforced aluminum alloy only. We perform a detailed analysis of the deformed specimen shapes to determine the dynamic yield strength. Additionally, hydrocode simulations of the Taylor impact tests using material models appropriate for the specimen material types are performed and compared to experimental data for model validation. This work provides the foundation for developing and validating robust MMC material models that may ultimately lead to innovative lightweight armor designs.

2. Experimental Methods

For the Taylor impact test method, a right circular cylinder is fired at high velocity onto a hard (rigid) surface, as shown in figure 1. This classic ballistic test was named after Sir G.I. Taylor who developed the test in 1948 to screen materials for ballistic applications during WW II. Taylor recognized that this experimental procedure permitted an estimate of a dynamic yield stress by measuring the overall length of the reference or original state of the cylinder and the final deformed specimen length (29). Although the test is relatively simple in theory, great attention must be given to maintaining planar impact of the cylinder on the rigid anvil and accurate post-mortem analysis (30).

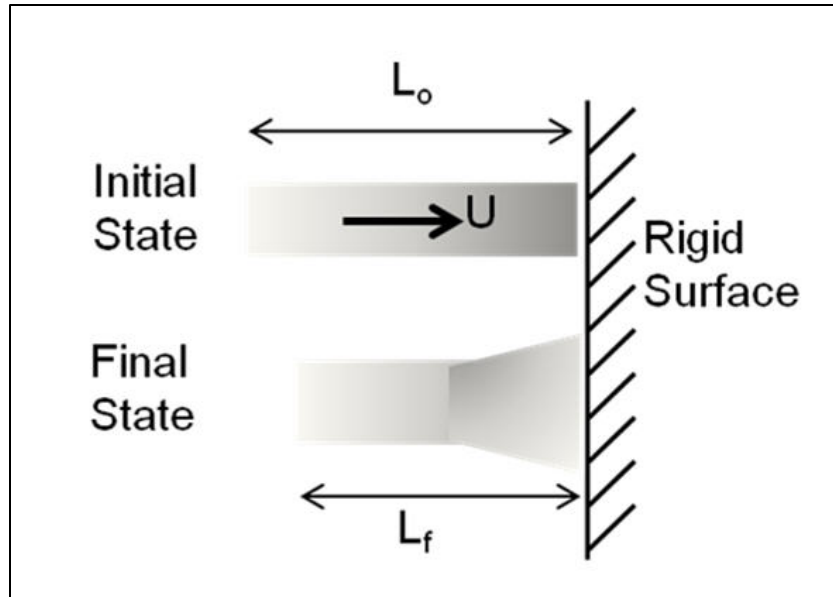


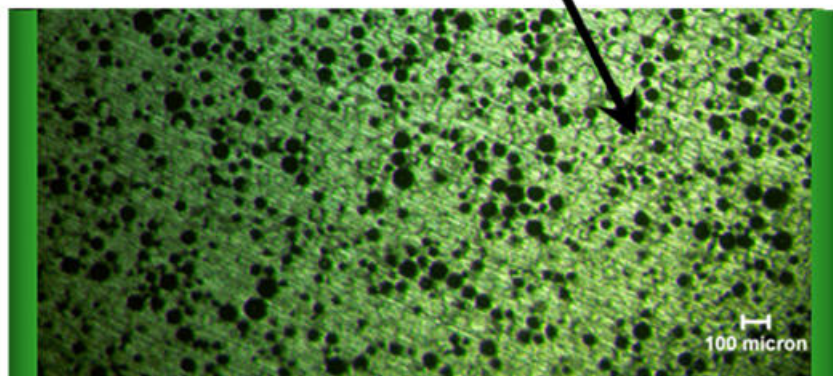
Figure 1. Original schematic of a Taylor impact test (from reference 1).

2.1 Materials, Equipment, and Procedures

2.1.1 Projectiles

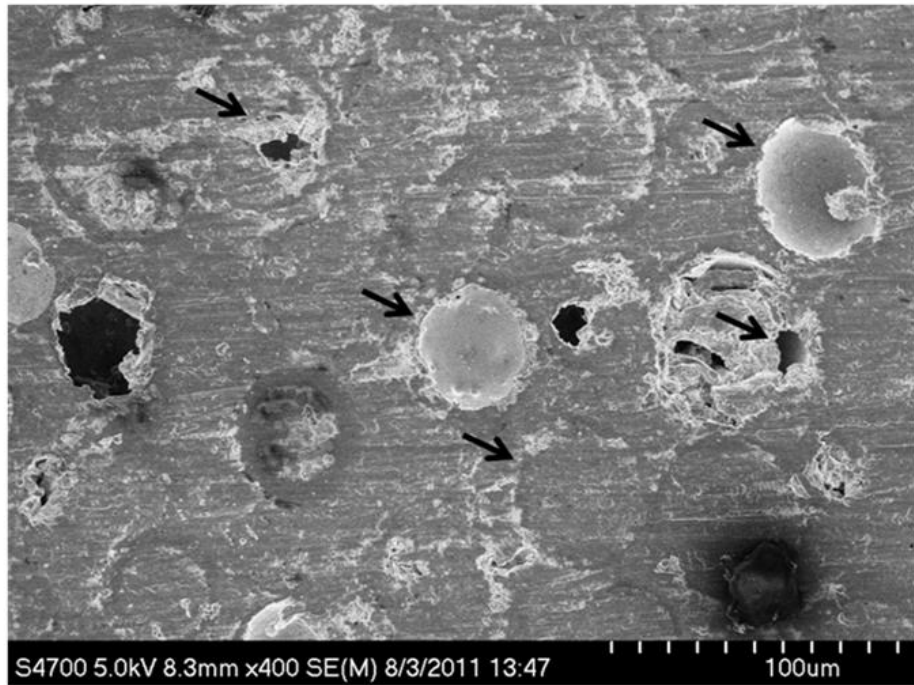
The particular MMC of interest consisted of an aluminum alloy (Al_2Cu) matrix with embedded ceramic spheres for reduced weight and strengthening. The matrix was cast with no subsequent heat treatment. The ceramic additives were predominantly hollow spheres made from silica, alumina, and iron. They are called ceramic cenospheres and are produced as a byproduct of burning coal (fly ash). The word ‘cenosphere’ comes from two Greek words: ‘kenos’ meaning hollow and ‘sphaira’ meaning sphere. The diameters of the cenospheres ranged between 10–106 μm with a density between 0.4–0.6 g/cm^3 , and they occupied approximately 20% of this composite by volume. Three different cylinder geometries were machined from a 17.8 \times 20.3 cm MMC plate that was 3.8-cm thick. It is noted that a solid aluminum face, approximately 1-mm thick, is cast into both plate surfaces as shown in figure 2. An undeformed ceramic sample was sectioned, etched, and polished for material imaging using a scanning electron microscope (SEM), as shown in figure 3a and b. Several features were determined using the SEM. Most notably, as shown in figure 3a with arrows: some of the aluminum “smeared” during polishing, some of the inclusions showed “leaks” (or voids) within the cenosphere or damage during sectioning, and some the inclusions were hollow while others appeared filled. One possible explanation is that during material processing, the lower viscosity liquid aluminum matrix infiltrated some hollow spheres and solidified upon cooling. An isolated cenosphere was magnified to obtain an approximate diameter of 15 μm and a wall thickness of approximately 3–5 μm , as shown in figure 3b.

Al₂Cu Matrix with embedded ceramic
spheres (~20% volume fraction)

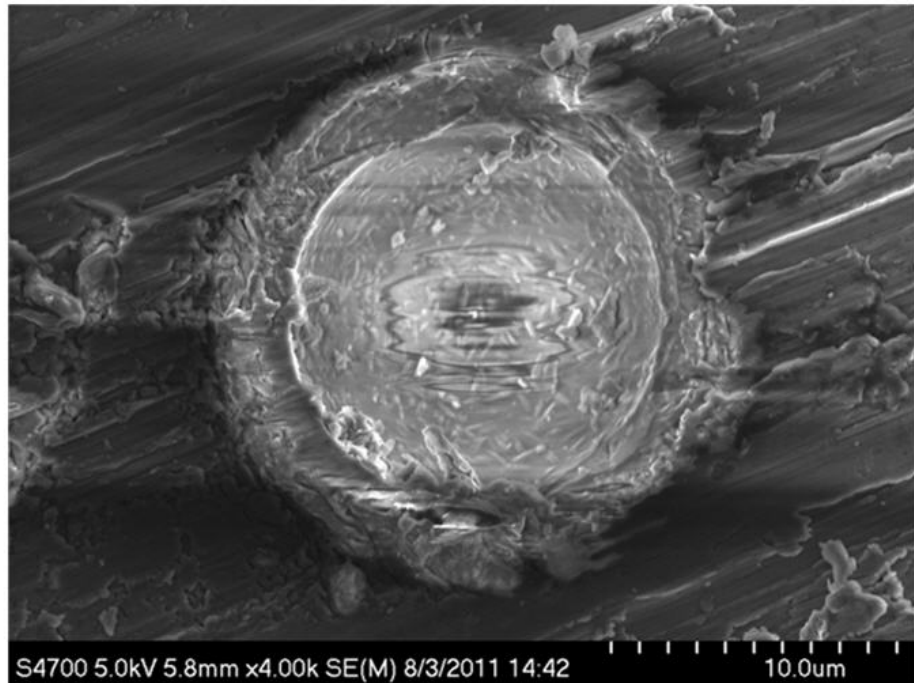


Solid Al Face

Figure 2. Schematic of the metal matrix composite.



(a)



(b)

Figure 3. SEM images of (a) the ceramic MMC showing spherical cenospheres ranging between 30–50- μm diameter, (b) magnified view of an isolated cenosphere with an approximate diameter of 15 μm and 3–5 μm wall thickness.

The MMC material plate was taken to the ARL welding shop and a water jet was used to machine-cut twenty-four 9.53-mm (24 each, 0.75-inch) diameter cylinders, twenty-nine 12.70-mm (29 each, 0.5-inch) diameter cylinders, and thirty-three 19.05-mm (33 each, 0.375-inch) diameter cylinders at right angles to the broad face of the plate. The length of all cylinders was held constant at 38.10 mm (1.5-inch original plate thickness). The cylinders were then weighed, fitted with elasto-foam launch sabots, and weighed again. Circumferential rings were scribed on some cylinders for high speed imaging, as shown in figure 4. The measured density of the ceramic MMC was 0.00214 g/mm^3 (2.14 g/cm^3) as compared with aluminum metal at 0.00270 g/mm^3 (2.7 g/cm^3). The elasto-foam launch sabot was determined to have a density of $4.585e-4 \text{ g/mm}^3$ (0.46 g/cm^3).

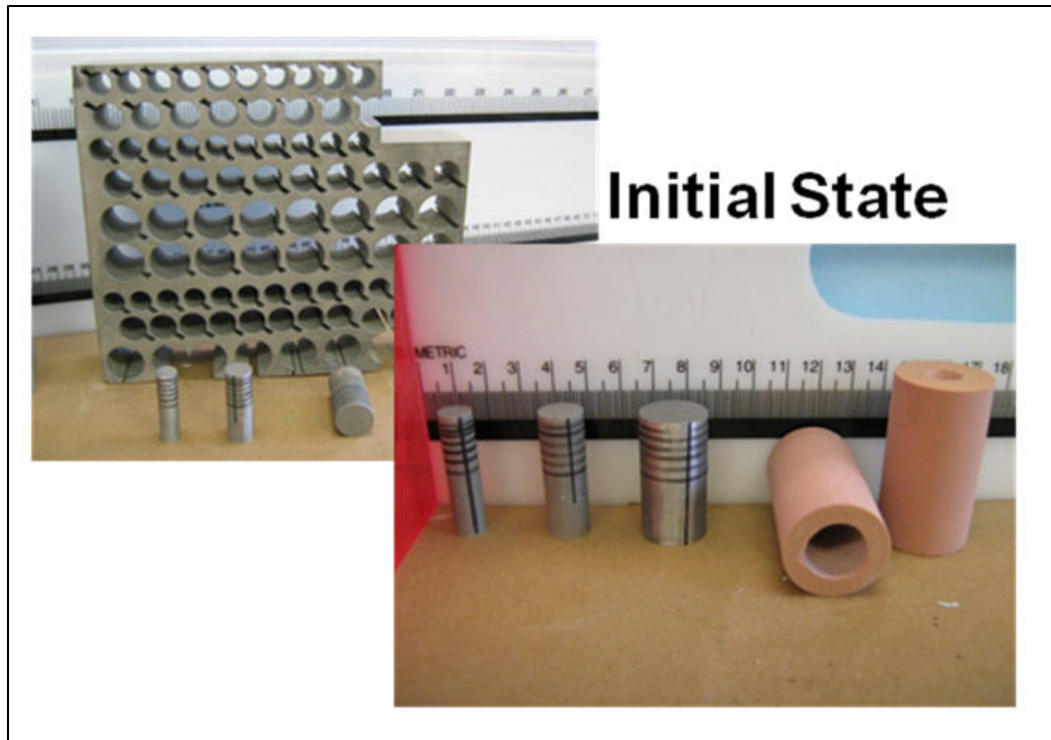


Figure 4. Ceramic MMC plate, cut cylinders and elasto-foam launch sabots.

2.1.2 Rigid Anvil

A ground steel high-hard plate was placed in front of a massive block of steel that was anchored to the gun table. After every shot, the high hard plate was examined and showed no deformation on the front (impacted) surface.

2.1.3 Instrumentation, Experimental Setup and Procedures

The following instruments/equipment was used in the Taylor impact investigation, as schematically shown in figure 5:

- 2.77-cm (1.09-inch) bore gas operated gun with a sabot stripping device
- Elasto-foam launch sabot
- Oscilloscope connected to two each beam lasers aligned with two each photovoltaic sensors
- 15.24-cm RHA steel block with a 1.27-cm thick high hard steel anvil plate

The following instruments/equipment was used to perform post-test analysis:

- SEM, optical microscope and polishing table

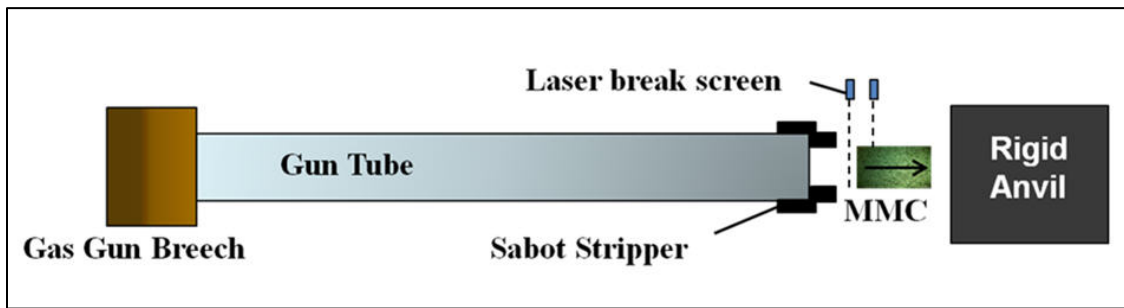


Figure 5. Schematic view of the assembly used for Taylor impact testing.

Gun Range 167 was prepared using the 2.77-cm bore gas operated gun, an RHA anvil block with a high hard steel faceplate that was surface polished, and a laser gate system to record the speed of all samples as they exited the gun barrel. Images of the full assembly and a magnified view of the laser gate system are shown in figure 6. The gate consisted of two beam lasers spaced 6.03 cm apart, located between the gun and anvil, and facing normal to the projected flight path. On the opposite side of the gun tube were two photovoltaic sensors receiving the laser beams and sending constant signals to an oscilloscope. Any object breaking the laser beams created a subsequent voltage drop on the oscilloscope, and the projectile speed could be calculated from the time difference between the separate voltage drops from the two sensors.

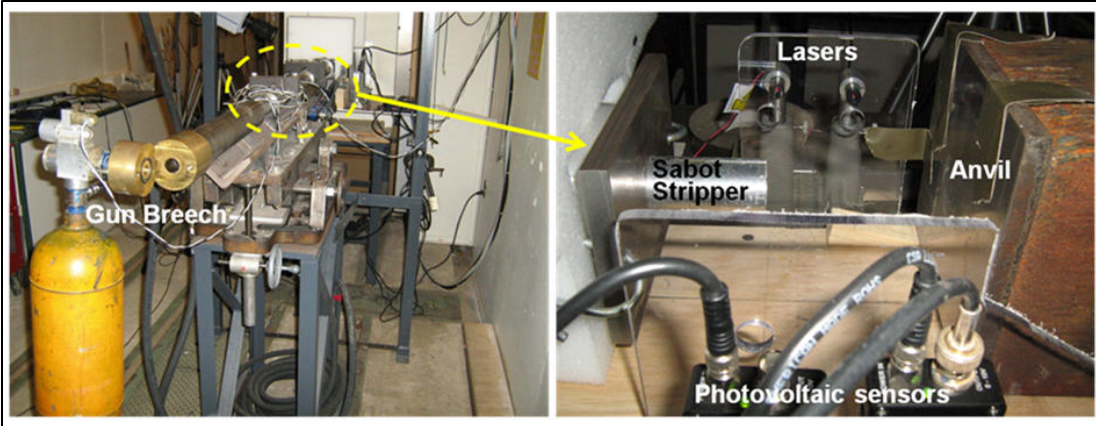


Figure 6. Photographic images of the Taylor impact test assembly including a view of the laser break screens.

The final launch package loaded into the gun included the sample projectile with an elasto-foam sabot that covered approximately 75% of the original projectile length. The sabot did not separate from the projectiles for the impact in the initial tests, which raised questions about the validity of any data collected. There were concerns of excess loading of the sample due to the extra momentum the sabot carried, as well as radial confinement of the sample, which would limit deformation. Both scenarios would give misleading data and therefore could not be used to estimate the dynamic yield strength or validate constitutive models implemented in hydrocodes. As a result, a device was conceptualized and manufactured to easily strip the sabot from the sample before exiting the gun barrel. The device consists of a single aluminum piece acting as an end-cap on the gun, as shown in figure 7a. Bolts and a plate with strong elastic cords secure the device in place. The device has a washer for the sabot to hit as it reaches the end of the gun, and a hole with an extended barrel for the sample to continue out and into the anvil, as shown in figure 7b. The hole is slightly bigger than the diameter of the projectile to support the sample and keep it stable after removal of the sabot. Inserts were designed to provide the proper diameter of this hole and enable the device to support all three sample diameters, as shown in figure 7b. This device discards the sabot before the velocity measurement and impact phenomena, and it keeps the projectile stable during the stripping process. Damage to the device during impact would occur primarily on the washer, which can easily be replaced after a shot.

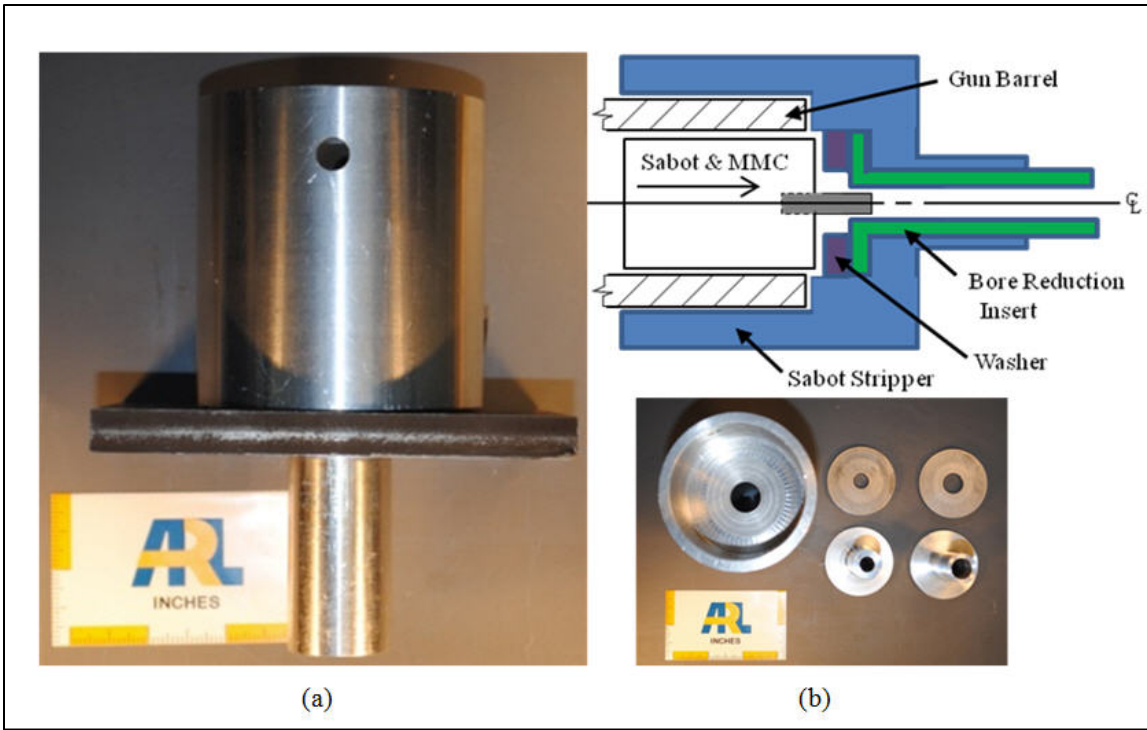


Figure 7. Sabot stripping device, (a) side view, (b) top view, with bore reduction inserts and schematic.

A parametric study was developed for three length over diameter (L/D) ratios (2, 3, and 4) shot at three different chamber pressures (0.52 MPa, 0.69 MPa, and 0.86 MPa) for a total of nine unique conditions. The impact velocity, final length, and foot diameter (noted as final diameter) were recorded for each sample and will be discussed in section 5. MMC samples fired at a pressure of 0.86 MPa showed prominent shear bands throughout and excessive fracturing at the foot diameter.

3. Analytical Consideration

Sir Geoffrey Ingram Taylor (1886–1975), Fellow of the Royal Society of Edinburgh, is considered one of the most creative and insightful scientists of the 20th century. In 1948 he published signature research on the Taylor impact test which involved the propagation of a plastic wave front in a solid material. The work was contained in three articles (with additional co-authors) that described theoretical considerations, tests on metallic materials and microstructural characterization (29–32). To determine an estimate of the dynamic yield stress using the final geometry of the deformed specimen, Taylor used the following simplifying assumptions:

1. Stress along the plastic wave front is constant and equal to the yield stress of the material.
2. Plastic-elastic boundary moves outwards at a uniform velocity from the impacted end.
3. Radial inertia is neglected, so the stress is considered as constant over any cross-section and the cylindrical projectile decelerates as a rigid body.

Together, assumptions one and two imply that the deceleration of the rear of the projectile is not uniform. Taylor and Whiffin recognized this limiting assumption and showed that dynamic yield stress was underestimated. This estimate of the yield stress was derived using the conservation of mass and momentum. Further, they provided a series of correcting factors in terms of the current length, L , which were tedious to obtain (29, 31). Whiffin (31) also showed that the yield strength was independent of the impact velocity using mild steel cylinders and the analysis of Taylor. In 1968, Hawkyard et al. (33) completed a simplified analysis for estimating flow stress using the conservation of energy and similar assumptions of Taylor. Wilkins and Guinan (34) then applied the estimated dynamic stress in a numerical simulation to determine the final deformed cylinder length and showed successful correlation with observed results. Using the energy approach as originally described by Hawkyard et al. (33), we assume that all of the projectile's kinetic energy, KE , is transferred to the projectile's internal energy, IE . We consider energy conservation to be written as,

$$KE + IE = \text{constant}, \quad (1)$$

where the kinetic energy evaluated at the initial state is,

$$KE = \frac{1}{2}mU^2, \quad (2)$$

and the internal energy is,

$$IE = \sigma_{YD} \int_{\bar{V}} \varepsilon d\bar{V}. \quad (3)$$

In equations 1–3, U is the impact velocity, \bar{V} is the current volume, m is the material mass, σ_{YD} is the dynamic yield strength, and ε is the current strain. Since the plastic front is considered steady and the flow stress is constant, the yield stress can be removed from the integral of plastic work in equation 3. Further assuming a uniform strain and using the original length, L_o , and the final deformed length, L_f , the integral becomes,

$$\int_{\bar{V}} \varepsilon d\bar{V} = \bar{V} \ln \left(\frac{L_f}{L_o} \right). \quad (4)$$

Placing equation 4 into 3 and substituting into equation 1 along with 2 gives,

$$\bar{V} \frac{1}{2} \rho U^2 = -\sigma_{YD} \bar{V} \ln\left(\frac{L_f}{L_o}\right). \quad (5)$$

Equation 5 can be solved for the dynamic yield stress to obtain,

$$\sigma_{YD} = -\frac{\rho U^2}{2 \ln\left(\frac{L_f}{L_o}\right)}. \quad (6)$$

Equation 6 can also be rearranged to provide estimates of the length

$$\frac{L_f}{L_o} = \exp\left(-\frac{\rho U^2}{2 \sigma_{YD}}\right). \quad (7)$$

Equation 7 describes the final-to-original length as a function of two material properties (ρ and σ_{YD}). Wilkins and Guinan (34) considered equation 7 to be a scaling law describing the deceleration of the projectile at various impact velocities.

The density, ρ , of the MMC material was determined by measuring the mass of each cylinder and dividing by the volume for a given radius, R_0 , using,

$$\rho = \frac{m}{\pi R_0^2 L_0}. \quad (8)$$

The density is only used in the initial kinetic energy calculation, so the nonuniform density profile due to the pure aluminum surface is not considered. Equations 6 and 7 describe the estimated dynamic yield stress and a scaling law for the deceleration of the cylindrical projectile at various impact velocities. Results for the cenosphere MMC material using the observed data and equations 6 and 7 will be given in section 5.

4. Numerical Simulations

Numerical modeling was performed on an eight-processor Linux computer using the hydrocode ALE3D (35), developed at Lawrence Livermore National Laboratory. The computational domain and the boundary conditions are shown in figure 8. An ALE3D input file was created describing the geometry, initial conditions, boundary conditions, and material response models. Analyses were conducted using a two-dimensional asymmetric geometry. Symmetry along the centerline was described by constraining the centerline nodes with no displacement in the radial direction. Also, the rigid wall was described by constraining the boundary nodes along the impacted end

with no displacement in the axial direction. The initial velocity of the projectile was the observed impact velocity. The governing equations for spatial and temporal deformation of the cylinder were solved using a Lagrangian formulation. Elements were approximately square with a mesh density of 0.49 mm/element in the z-direction and 0.35 mm/element in the r-direction. The consistent units used for all numerical simulations were g, mm, msec, and MPa.

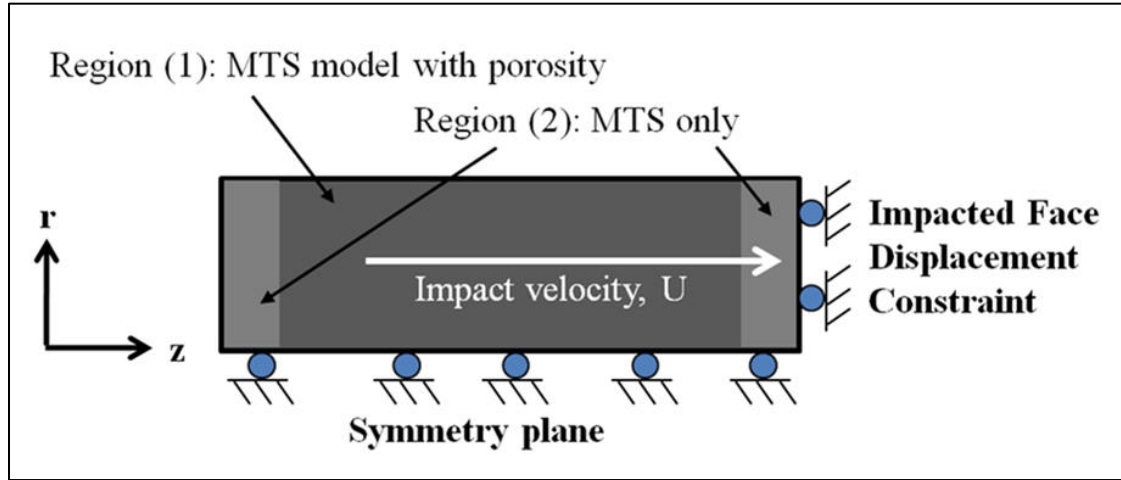


Figure 8. Schematic illustrating the reference configuration, initial conditions, boundary conditions and description of material response for the cenospheres MMC Taylor Impact Test. Note, the MMC material contained two distinct regions: (1) end-caps of aluminum only and (2) aluminum matrix with cenosphere inclusions. These regions were taken into account in the numerical modeling.

In order to account for the layer of solid aluminum along the impacted end, the computational domain for the projectile was divided into two regions for the MMC material. Both regions used the same material strength model; however, the MMC region used a yield surface model for porous materials to account for the inclusions (36). The material parameters for the MMC as well as the matrix-only aluminum alloy were unknown. As a preliminary numerical investigation, it was decided to use available parameters for 6061-T6 Al and examine the validity of our novel numerical approach by comparisons with observed cylinder deformations. The aluminum matrix in the MMC was not 6061-T6 Al. Since the matrix-only alloy was not provided for strain rate dependant material response testing during the time of this investigation, we chose 6061-T6 to represent the matrix because it is representative of a non-ferrous light aluminum alloy metal and because of availability of various constitutive models with reliable material parameters for 6061-T6.

ALE3D is a large deformation continuum mechanics code that contains a material strength formulation. Typically, the strength formulation can be subdivided into five parts: (1) a stress/strain relationship for elastic material response, (2) a yield surface that specifies the multiaxial stress state corresponding to the start of plastic flow, (3) a flow rule that describes plastic behavior after yielding by relating strain increments to stress increments, (4) a consistency statement that constrains the stress state to remain on the yield surface during plastic

flow, and (5) a hardening rule that describes the evolution of the flow strength during plastic deformation. The constitutive relation or flow rule physically describes material response by relating stresses to deformations. The finite element framework mathematically connects kinematics and field equations with boundary conditions. Most generally, a constitutive relation for the material flow strength, $\bar{\sigma}$, can be written as some function,

$$\bar{\sigma} = \tilde{\sigma}(\varepsilon, \dot{\varepsilon}, T, p, \beta), \quad (9)$$

ε is the plastic strain in the current configuration, $\dot{\varepsilon}$ is the plastic strain rate, T , the temperature, p , the pressure, and β is some internal state variable. Most empirical constitutive models (e.g., Johnson-Cook strength model) are constructed on macroscopic material response tests and do not track a state variable; they are written as,

$$\sigma = \sigma(\varepsilon, \dot{\varepsilon}, T, p). \quad (10)$$

Several phenomenological constitutive models attempt to provide a better representation of the underlying physics. The Mechanical Threshold Stress (MTS) model, introduces threshold stress terms, $\hat{\sigma}_i$, as internal state variables describing structure evolution. The flow stress can now be described as,

$$\bar{\sigma} = \tilde{\sigma}(\dot{\varepsilon}, T, p, \hat{\sigma}_i). \quad (11)$$

The threshold term was introduced in the material flow stress referring to a measure of the strength for a changing material microstructure during plastic flow.

The MTS model uses grain level strengthening mechanisms where the flow stress is defined by the resistance to the motion of dislocations introduced by various microstructural barriers (17, 38–42). Barriers implemented in the model include interactions within a forest of dislocations (dislocation-dislocation interaction), interstitial and solute lattice distortions (dislocation-interstitial/atomic interaction), stress concentrations at grain boundaries (grain size strengthening), and so on. For a given strain rate, each dislocation interaction contributes an individual threshold stress, $\hat{\sigma}_i$, that are all added together to obtain the macroscopic flow resistance of the material. The individual threshold stresses are contained in rate dependant mechanisms controlling the kinetics of deformation. Currently, there are two classes of mechanisms within MTS: an athermal process (not sensitive to temperature change) and thermal activation controlled deformation processes. The athermal deformation process primarily considers contributions due to “Hall-Petch”-like grain boundary strengthening.

For dislocation interaction with some energy barrier “ i ”, we can write equation 11 as

$$\sigma = \hat{\sigma}_a + \frac{\mu(T,p)}{\mu_0} \sum_{i=1}^n \hat{\sigma}_i S_i(\dot{\varepsilon}, T, p), \quad (12)$$

where $\hat{\sigma}_a$ is the athermal threshold stress considered to be constant, $\hat{\sigma}_i$ are thermally activated thresholds that may evolve, S_i are constant-structure deformation terms that are mainly a function of strain rate, $\dot{\varepsilon}$, and temperature, T. We consider μ to be the temperature-dependant shear modulus and μ_0 is the reference shear modulus. Individual thermally activated processes can include dislocation interactions with solute atoms (interstitials), second phase precipitates, interaction with another dislocation as well as forest dislocation strengthening (which is not athermal).

For our application, the summed threshold stress term includes two parts and equation 12 is written as

$$\bar{\sigma} = \hat{\sigma}_a + \frac{\mu(T,p)}{\mu_0} [\hat{\sigma}_{int} S_{int} + \hat{\sigma}_e S_e]. \quad (13)$$

The first term in equation 13 is an athermal threshold stress representing dislocation-grain boundary interactions (long-range barriers), in the second part $\hat{\sigma}_{int}$ is a constant strength due to interstitials or barriers to thermally activated dislocation motion, and $\hat{\sigma}_e$ is the thermally activated strain hardening component of the flow stress. The scaling factors S_{int} and S_e are temperature and strain rate dependent determined through an Arrhenius rate equation and take the form

$$S_{int} = \left[1 - \left(\frac{k_b T}{g_{0,int} b^3 \mu(T)} \ln \frac{\dot{\varepsilon}_{0,int}}{\dot{\varepsilon}} \right)^{1/q_{int}} \right]^{1/p_{int}} \quad (14)$$

where k_b is the Boltzmann constant, b the burgers vector, $g_{0,int}$ and $g_{0,e}$ are activation energies for the interstitial and strain hardening components, respectively, $\dot{\varepsilon}_0$ is a reference strain rate, and q_{int} , p_{int} , q_e , p_e are empirical constants related to an “obstacle profile” (38, 39).

It is important to note that the strain hardening response in the evolution equation is strain rate dependant and is typically given by a saturating hardening law. MTS is the only constitutive model implemented in hydrocodes that has this unique feature. Consequently hardening is not defined in terms of plastic strain within MTS. It is implicitly determined from the dislocation density (or structure) evolution using $\hat{\sigma}_e$ transition between two limiting structure regimes. Further details on MTS can be obtained by reviewing the work Maudlin et al. 1997; Follansbee and Kocks, 1988; Maudlin et al., 1990; Goto et al., 2000; Banerjee, 2007; Regazzoni et al., 1987; and Mecking and Kocks, 1981 (17, 37–42).

The physics-based MTS model was used for all simulations to describe the flow strength of the deforming cylindrical MMC projectile. Also, the Gurson yield surface model was used with the MTS model in order to account for the porosity of the inclusions in the MMC region (36). The rationale was that the hollow ceramic spheres in the MMC material would fracture in a brittle manner and behave similar to the pores in the model, given appropriate parameters. The material

had a void fraction of 20%, which was one of the history variables associated with the Gurson model. The yield condition, \emptyset , in the Gurson model was modified by Tvergaard (43, 44) and Tvergaard and Needleman (45) by introducing three fitting parameters q_i (for $i = 1, 2, 3$) determined from finite element analysis of a unit cell with an initially spherical void. Using Tvergaard's modification, the Gurson yield condition can be written as

$$\emptyset = \frac{\sigma_{vm}^2}{\bar{\sigma}^2} + 2fq_1 \cosh \left\{ \frac{q_2}{2} \frac{3}{2} \frac{p}{\bar{\sigma}} \right\} - (1 + q_3 f^2) = 0 \quad (16)$$

where σ_{vm} is the von Mises effective stress, p is the pressure and f is the void fraction volume (porosity function). Note, in equation 16 that flow strength, $\bar{\sigma}$, is obtained from the MTS material response model while the effective stress, σ_{vm} , is obtained from the field equations (stress tensor piece). The Gurson model is essentially a porosity modification to J_2 -flow theory ($\sigma_{vm} = \sqrt{3J_2}$ where J_2 is the second deviatoric stress invariant). The yield condition in equation 16 becomes the von Mises yield criteria when $f = 0$. The ALE3D version includes provisions for void nucleation and failure triggers associated with the coalescence of voids (46). For our application, we suppressed the nucleation and failure triggers but allowed the void fraction to continue to evolve and collapse.

First, the ALE3D hydrocode was run using a matrix-only material input file to replicate published Taylor impact tests for 6061-T6 Al. The MTS parameters used for the 6061-T6 alloy were obtained from G. T. (Rusty) Gray's MST-8 team at Los Alamos National Laboratory (47) and are given in the appendix as used for ALE3D MTS input. The goal was to compare the final deformed state with the observed to validate parameters used for 6061-T6 Al in the MTS model. The MTS parameters obtained for 6061-T6 aluminum provided excellent agreement (within 2% of the experiment) with the Taylor impact test on 6061-T6 aluminum alloy data completed by House et al. (48). After this was achieved, the same MTS model parameters for 6061-T6 Al with a Gurson yield surface model were used to compare with the observed deformed state of the MMC material (end-caps and matrix with inclusions from the Taylor cylinder impact test). Numerical simulations using the MTS model with a von Mises yield criteria (end-caps and the matrix with no inclusions) were also completed and compared with the Gurson to show the influence of porosity. All of the numerical results including those obtained with the MTS and Gurson models for the MMC are discussed in section 5.

5. Results

Table 1 provides the test matrix for the Taylor impact tests performed using aluminum matrix ceramic cenosphere specimens striking a polished rigid high-hard steel plate. The statistically determined density obtained by weighing each sample prior to testing was $2.14e-3$ g/mm³ with a standard deviation of 7%. The statistical variation of the cenosphere particle distribution for the

received MMC plate was not accounted for so, spatial density variation was expected. After an experiment, the recovered specimen was subjected to post-mortem analysis that included measuring the final diameter at the impacted surface (footprint) and the final length as given in table 1. In some cases the recovered specimens were sectioned and polished for microscopy. The tests performed to date have shown trends similar to those of Wilkins and Guinan (34) observed for several metals. For example, figure 9 provides a similar result suggesting that $L_{final}/L_{original}$ may be independent of the initial length for a given specimen aspect ratio; however, more testing is required to infer a conclusion.

Table 1. Experimental data and test results for impacts of aluminum matrix with cenospheres particles (metal matrix composite).

Initial Diameter	Length/Diameter Ratio (L/D)	Chamber Pressure	Impact Velocity	Specimen Mass	Launch Package Mass	Mean Dynamic Yield Stress	Final Length	Final Diameter (Impacted foot)
[mm]		[MPa]	[m/s]	[g]	[g]	[MPa]	[mm]	[mm]
9.53	4	0.52	194.68	6.30	19.00	264.20	32.26	14.99
		0.69	235.37	5.20	13.30	278.72	31.50	16.51*
		0.86	236.71	6.60	19.50	343.20	31.24	17.78*
12.70	3	0.52	154.47	9.90	22.70	232.27	34.29	17.27
		0.69	189.84	10.10	22.40	216.28	32.00	18.29
		0.86	243.89	9.40	20.20	269.61	30.73	17.02*
19.05	2	0.52	153.01	23.60	34.20	292.38	34.93	24.13
		0.69	174.94	24.10	35.50	282.32	33.78	26.16*
		0.86	201.67	22.90	32.60	335.46	33.53	27.05*

Note: *Fracture or petalling observed at impacted foot (base) of cylinder.

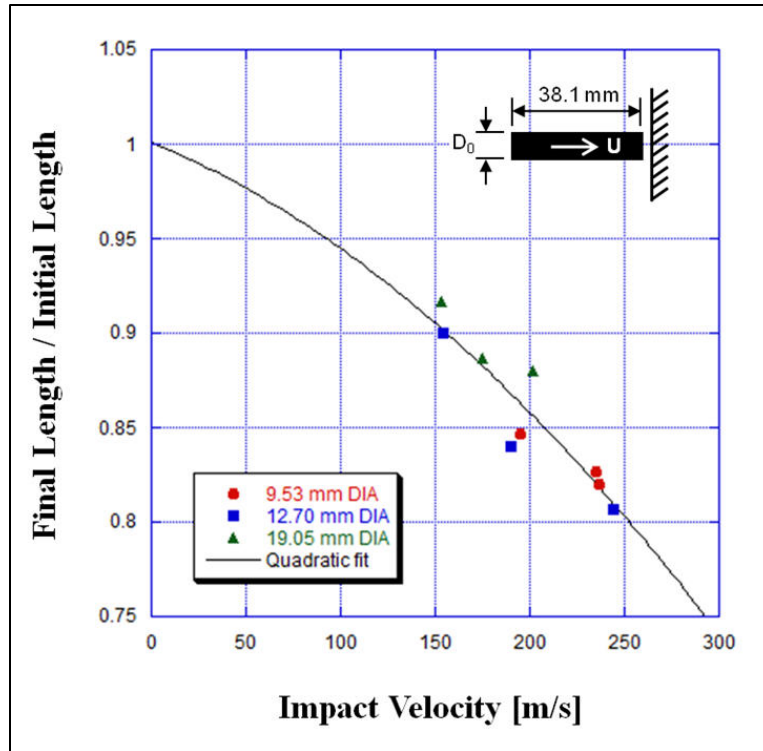


Figure 9. Observed results illustrating the dependence of final deformed length of the aluminum-ceramic cenosphere MMC to the original length.

The observed results were also used in equation 6 to obtain the dynamic yield stress listed in table 1. The MMC material work hardens; therefore, the material strength increases with impact velocity and plastic strain. The plastic wave front in the MMC propagates in the early stages of the impact to an approximately fixed position close to the rigid boundary. The final deformed shapes of the MMC specimens tested are shown in figure 10. At higher chamber pressures and impact velocities, the material fractures due to large hoop strains, resulting in radial cracks and “petals” at the impacted end of the specimen length, are shown in figure 10b and c. Figure 11 illustrates that for the MMC the $L_{\text{final}}/L_{\text{original}}$ ratio scales with strength, density, and impact velocity. Similar results were observed by Wilkins and Guinan (34) for metals.

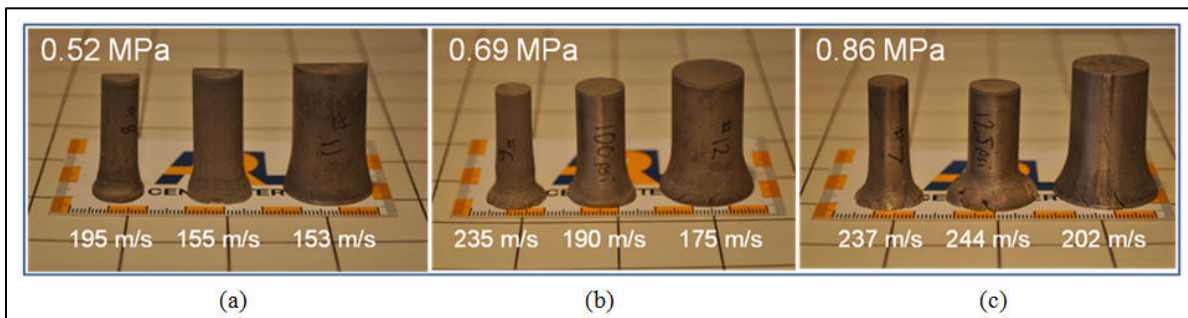


Figure 10. Side profiles of the final deformed shapes for the MMC specimens from Taylor Impact tests using three different chamber pressures and specimen diameters.

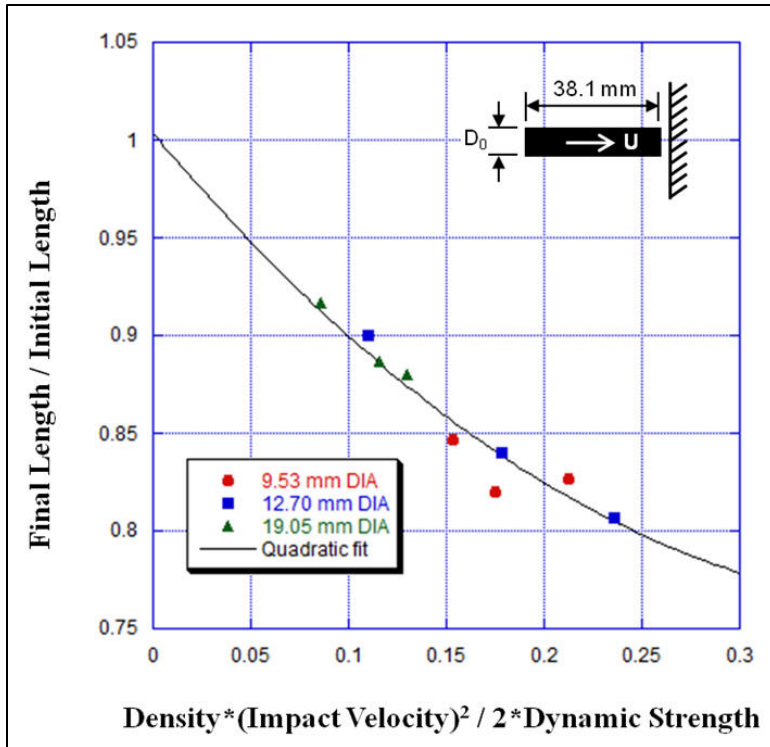


Figure 11. Observed results for MMC Taylor tests illustrating that final length deformed as a function of the density, strength, and impact velocity.

A comparison of the numerical results with experiments are given in table 2. The MMC material response approach using a von Mises yield surface with the MTS model parameters over-predicted the final length by 6% and under-predicted the final footprint diameter by 57%. The final length was over-predicted by 5% and the footprint diameter prediction improved to 25% error by accounting for the cenosphere porosity using the Gurson yield surface model with MTS. At lower impact velocities the improvement was not as dramatic and this was probably due to the influence of constraint at the end-cap and reduced pore collapse in the MMC region.

Table 2. Comparison of predicted with observed results for 6061-T6 aluminum alloys (47) and the metal matrix composite.

Material Impacted	Initial Diameter [mm]	L/D	Impact Velocity [m/s]	Final Diameter			Final Length		
				EXP	MTS	MTS / Gurson (%err)	EXP	MTS	MTS / Gurson (%err)
6061-T6 Al	7.60	2	240	10.67	10.41 (2%)	N/A	12.95	13.21 (2%)	N/A
MMC	9.53	4	195	14.99	6.35 (57%)	11.18 (25%)	32.26	34.29 (6%)	34.04 (5%)
MMC	12.70	3	190	18.29	16.26 (11%)	14.99 (18%)	32.00	34.54 (8%)	35.31 (10%)

Differences in plastic strain evolution using the Gurson yield surface as opposed to the von Mises yield criteria are shown in figure 12. By accounting for cenosphere porosity and collapse, the location of greatest plastic strain moved away from the specimen/rigid surface interface region into the MMC/end-cap interface region, which is within the specimen itself. The region of plastic strain is larger along the length and more uniform radially with the Gurson yield surface, as shown in figure 12. The porous MMC material exhibits an energy dissipating volume change that is not available in fully dense materials.

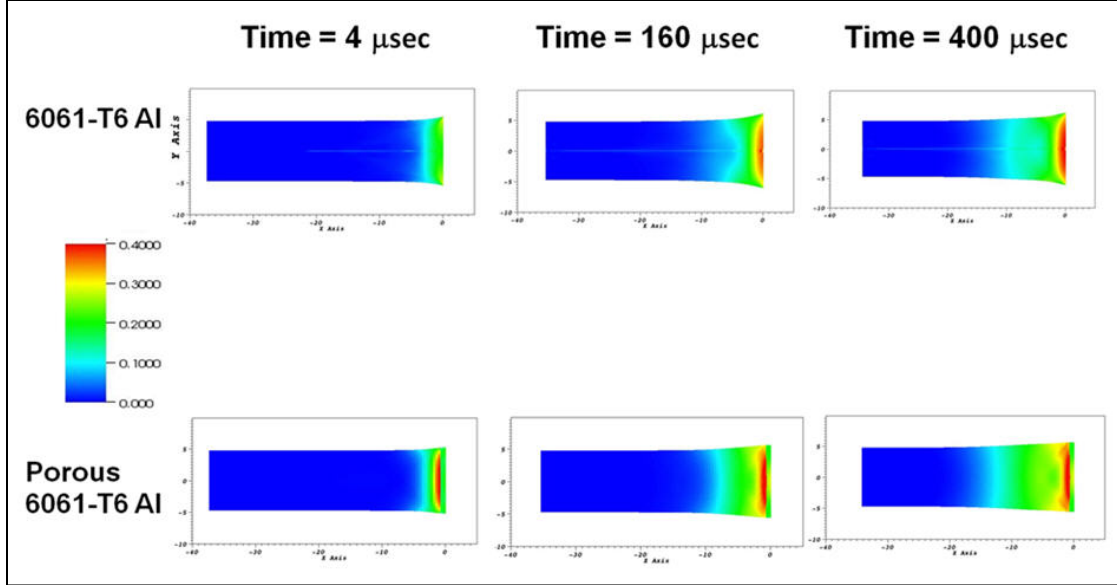


Figure 12. Comparison of plastic strain evolution using the von Mises (top) and Gurson yield surface (bottom) models for the aluminum matrix-ceramic cenosphere region with aluminum-only end-caps.

Some of the final deformed cylinders were sectioned and polished for microstructural evaluation. Figure 13 shows a sectioned specimen and three regions where samples were prepared for optical microscopy. In the downstream non-impacted region where the MMC did not undergo significant plastic strain, the cenosphere ceramic inclusions retained their original uniform spherical shapes, as shown in figure 14. Notice also, that some spheres shown in figure 14 are not hollow and were probably filled with aluminum during processing. The spherical dark regions in figure 14 are either sectioned inclusions or inclusions that were removed during sectioning/polishing.

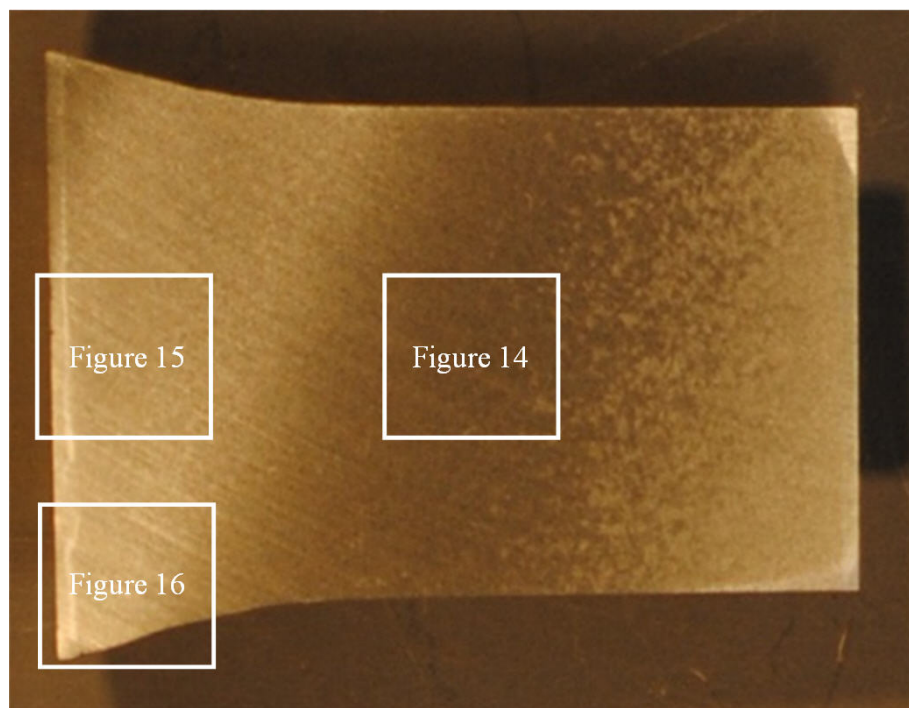


Figure 13. Macroscopic sectioned view of deformed specimen and boxed regions for optical imaging.

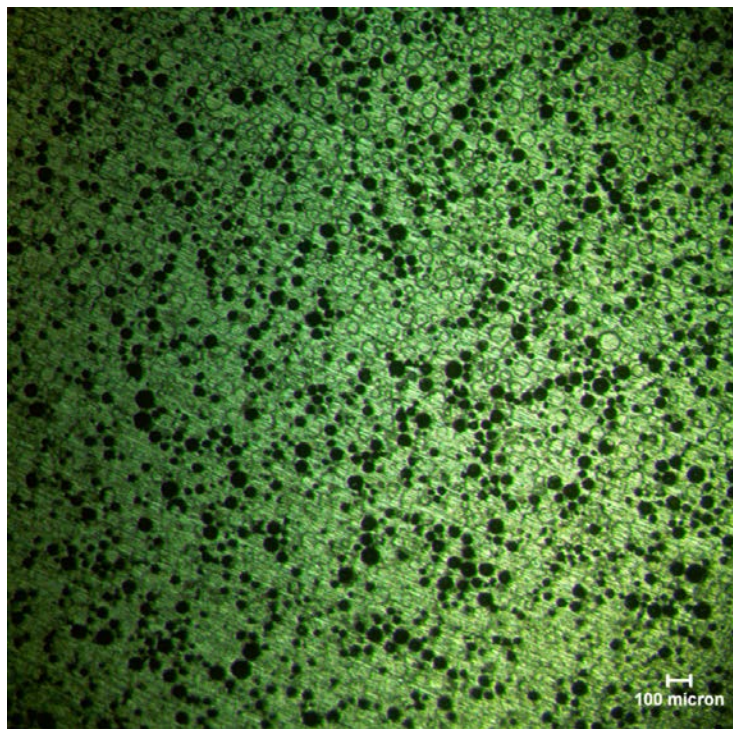


Figure 14. MMC material microstructure of non-deformed region. Note the uniform spherical shapes of the inclusions; some spheres are not hollow and filled with aluminum and the dark regions are either sectioned inclusions or inclusions that were removed during sectioning/polishing.

Micrographs of the impacted regions are shown in figures 15 and 16. The low porosity region, shown in these figures on the far left, is the aluminum matrix-only end-cap. Immediately past the matrix-only region the ceramic inclusions are not spherical but rather more closely resemble oblate spheroids. The numerical results using the MTS/Gurson modeling approach revealed pore collapse near the impacted face. At the rear of the projectile, the porosity remained at the original 20%, but closer to the impacted face, the porosity decreased. Closer to the impacted face around the center line, the calculation predicts that the porosity had dropped to half its original value, as shown in figure 17. Evidence of this mechanism was revealed by comparing the micrograph in figure 14 with figures 15 and 16. Notice in figures 15 and 16 that the hollow cenosphere profiles have changed from spherical on the lightly strained right side to oval in the mid-region and near the surface, there is a marked decrease in void fraction toward the impacted face. These compressed dark regions represent crushed pores/voids near the highly strained impacted surface.

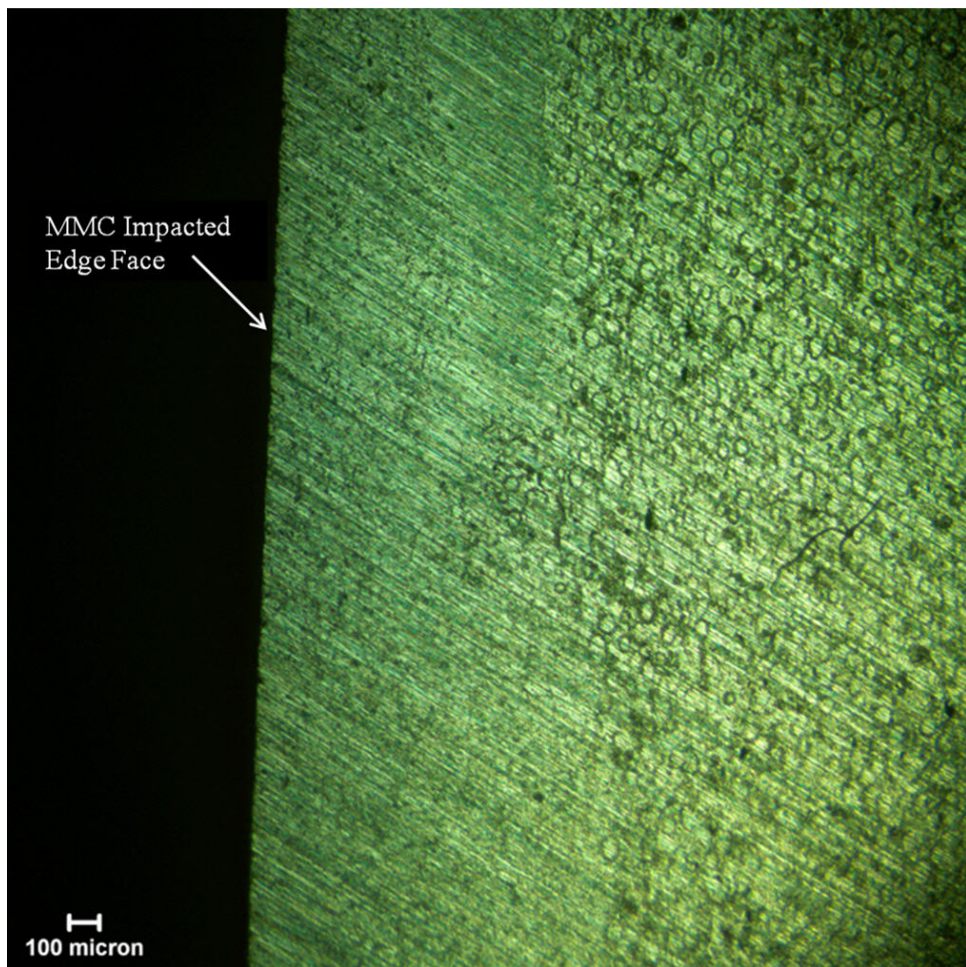


Figure 15. Micrograph of the MMC material in the mid-radial region (centerline) toward the impacted face. The low porosity region on the far left is the aluminum matrix-only end-cap. Note that the cenosphere profiles are changing from spherical on non-deformed right side to oval in the mid-region.

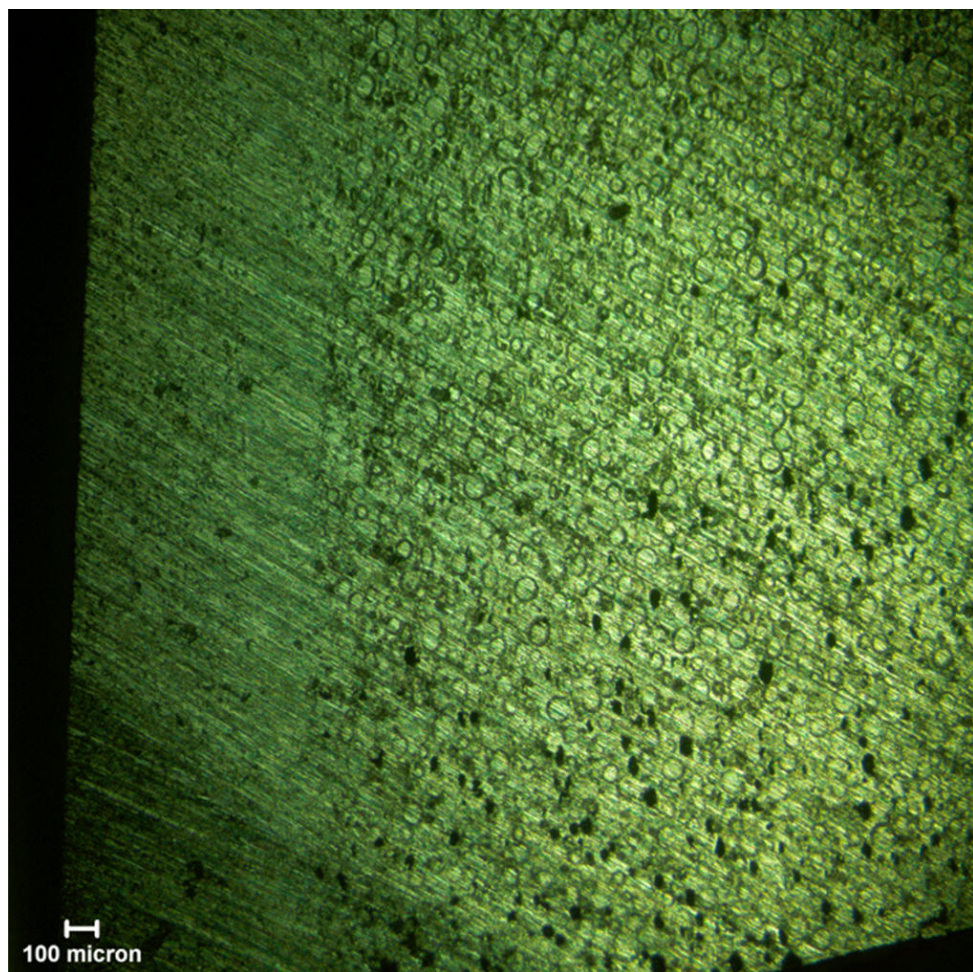


Figure 16. Micrograph of the MMC material in high strained corner area. The cenosphere near the end-cap/MMC interface are clearly collapsing during impact. The dark regions represent crushed pores/voids.

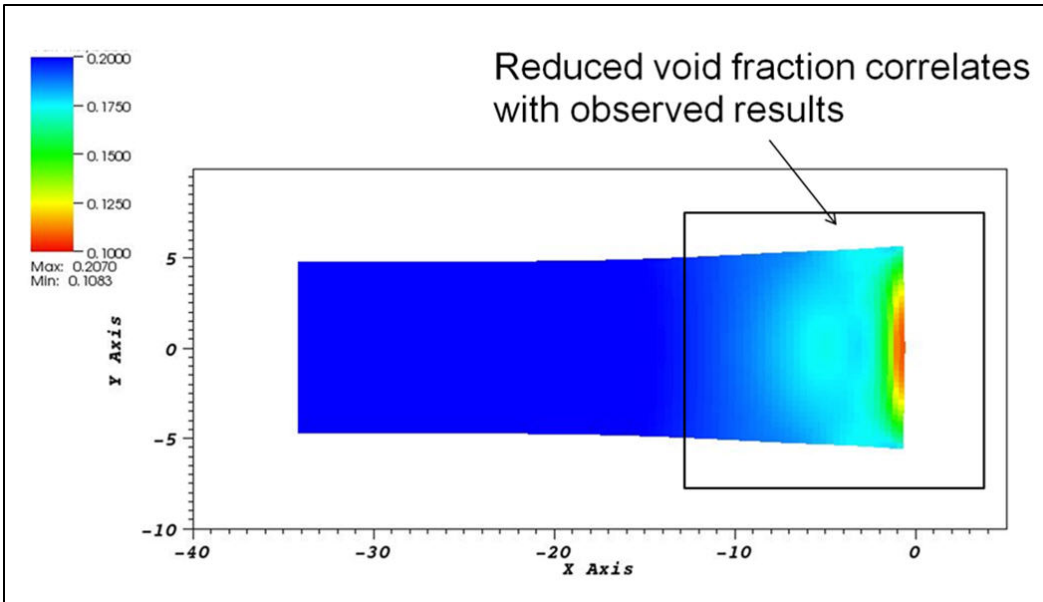


Figure 17. Evolution of porosity using the Gurson yield surface model for the aluminum matrix-ceramic cenosphere region. Note, the end-cap region was not shown in contour plot but was included in the numerical simulation.

6. Summary and Conclusions

Taylor Impact Tests involving an aluminum matrix with ceramic cenosphere inclusions provided data that can be used for validating material models, as well as estimating material properties such as dynamic yield strength. It was determined that using the MTS model with the Gurson yield surface for describing the material response of the MMC region has the capability to more accurately predict the behavior of MMC as compared to using MTS with the von Mises yield criteria. The rigid impact experiments performed revealed that although this particular MMC was relatively soft, the cenospheres provided energy absorbing features along with a reduction in weight. Energy absorption was not clear in the results but we suggest that it is related to the length of the deformed cylinder and the strength of the inclusions. Similar observations have been indicated by Clayton (49) and Williams (50). From a numerical standpoint at the continuum level, the addition of a porosity model is required to describe this material response. As a preliminary numerical investigation, an MTS constitutive model with the Gurson yield surface model provided an encouraging framework for describing MMC high strain rate behavior. Possible alternatives to this specific model combination still need to be investigated, and most of the parameters specific to this material still need to be generated. However, the results of this investigation provide an invaluable direction for future modeling efforts, as well as for validating the resulting material models and model parameters for this class of metal matrix composites. This mechanism may be an important feature for shock mitigation and dissipation.

7. References

1. Reed, H., Ed. *Ballisticians in War and Peace: A History of the United States Army Ballistic Research Laboratory*; Vol. 3; U.S. Army Research Laboratory: Aberdeen Proving Ground, MD, 1992.
2. Burns, B., Ed. *Advanced Ballistics Science and Engineering*; U.S. Army Research Laboratory: Aberdeen Proving Ground, MD, 2008.
3. Zukas, J., Ed. *High Velocity Impact Dynamics*; Wiley-Interscience Publication, 1990.
4. Chou, P. C.; Hopkins, A. K., Ed. Dynamic Response of Materials to Intense Impulsive Loading; Library of Congress Catalog Card Number 73-600247, 1973.
5. Benson, D. J. Computational Methods in Lagrangian and Eulerian Hydrocodes. *Comp. Methods in Appl. Mech. And Engg.* **1992**, *99*, 235–394.
6. Zukas, J. A.; Scheffler, D. R. Practical Aspects of Numerical Simulations of Dynamic Events: Effects of Meshing. *Int. J. Imp. Engg.* **2000**, *24*, 925–945.
7. Johnson, G.R. Numerical Algorithms and Material Models for High-Velocity Impact Computations. *Int. J. Imp. Engg.* **2011**, *38*, 456–472.
8. Field, J. E.; Walley, S. M.; Bourne, N. K.; Huntley, J. M. Experimental Methods at High Rates of Strain. *J. De Physique IV* **1994**, *4*, C8 3–C8 22.
9. Rohr, I.; Nahme, H., Thoma K. Material Characterization and Constitutive Modelling of Ductile High Strength Steel for a Wide Range of Strain Rates. *Int. J. Imp. Engg.* **2005**, *31*, 401–433.
10. Segletes, S.; Zukas, J. Simulation of High Strain Rate Effects with Microcomputers. *Proceedings of the International Conference of Mechanical Properties of Materials at High Rates of Strain*, Oxford, UK, 1989.
11. Johnson, G. R.; Hoegfeldt, J. M.; Lindholm, U. S.; Nagy, A. Response of Various Metals to Large Torsional Strains Over a Large Range of Strain Rates – Part 1: Ductile Metals. *J. Engg. Matls. Tech.* **1983**, *105*, 42–47.
12. Johnson, G. R.; Hoegfeldt, J. M.; Lindholm, U. S.; Nagy, A. Response of Various Metals to Large Torsional Strains Over a Large Range of Strain Rates – Part 2: Less Ductile Metals. *J. Engg. Matls. Tech.* **1983**, *105*, 48–53.

13. Johnson, G. R.; Cook, W. H. A Constitutive Model and Data for Metals Subjected to Large Strains, High Strain rates and High Temperatures. *Proceedings of the 7th International Symposium on Ballistics*, Hague, Netherlands, 1983.
14. Johnson, G. R.; Cook, W. H. Fracture Characteristics of Three Metals Subjected to Various Strains, Strain Rates, Temperatures and Pressures. *Engg. Frac. Mech.* **1985**, *1*, 31–48.
15. Zerilli, F. J.; Armstrong, R. N. Dislocation-Mechanics-Based Constitutive Relations for Material Dynamics Calculations. *J. Appl. Phys.* **1987**, *61*, 1816–1825.
16. Maudlin, P. J.; Bingert, J. F.; House, J. W.; Chen, S. R. On the Modeling of the Taylor Cylinder Impact Test for Orthotropic Textured Materials: Experiments and Simulations. *Int. J. Plas.* **1999**, *15*, 139–166.
17. Maudlin, P. J.; Foster, J. C.; Jones, S. E. A Continuum mechanics Code Analysis of Steady Plastic Wave Propagation in the Taylor Test. *Int. J. Imp. Engg.* **1997**, *19* (3), 231–256.
18. Predebon, W. W.; Anderson, C. E.; Walker, J. D. Inclusion of Evolutionary Damage Measures in Eulerian Wavecodes. *Comp. Mech.* **1991**, *7*, 221–236.
19. Johnson, G. R.; Stryk, R. A.; Holmquist, T. J.; Souka, O. A. Recent EPIC Code Developments for High Velocity Impact: 3D Element Arrangements and 2D Fragment Distributions. *Int. J. Imp. Engg.* **1990**, *10*, 281–294.
20. Ramesh, K. T.; McCauley, J. W. *USARL Material Center of Excellence Collaborative Research Program on Advanced Metals and Ceramics for Armor and Anti-Armor Applications*; ARL-CR-576; U.S. Army Research Laboratory: Aberdeen Proving Ground, MD, 2006.
21. Ibrahim, I. A.; Mohamed, F. A.; Lavernia, E. J. Particle Reinforced metal Matrix Composites – A Review. *J. Matl. Sci.* **1991**, *26*, 1137–1156.
22. Aghajanian, M. K.; McCormick, A. L.; Marshall, A. L.; Waggoner, W. M.; Karandikar, P. K. Static and Dynamic Properties of Mg/Ceramic MMCs. *Proceedings of the 34th International Conference on Advanced Ceramics and Composites*, Daytona Beach, FL, 2010.
23. Chang, H.; Binner, J.; Higginson, R. Ballistic Evaluation and damage Characterization of Metal-ceramic Interpenetrating Composites for Light Armor Applications. *Proceedings of the 34th International Conference on Advanced Ceramics and Composites*, Daytona Beach, FL, 2010.
24. Heidenreich, B.; Crippa, M.; Voggenreiter, H.; Gedon, H.; Nordmann, M. Development of Biomorphic SiSiC- and C/SiSiC-Materials for Lightweight Armor. *Proceedings of the 34th International Conference on Advanced Ceramics and Composites*, Daytona Beach, FL, 2010.

25. Mofet-Etzion Yehuda. <http://www.mofet-etzion.co.il/>; last accessed October 2012.
26. Exote. <http://www.exote-armour.com/>; for details choose link on main page for Exote-Armour/Material last accessed October 2012.
27. Wilkins, M. L.; Cline, C. F.; Honodel, C. A. *Fourth Progress Report of Light Armor Program*; UCRL-50694; Lawrence Radiation Laboratory: Livermore, CA, 1969.
28. Gooch, W. A.; Burkins, M. S.; Palicka, R.; Rubin, J.; Ravichandran, R. Development and Ballistic Testing of a Functionally Graded Ceramic/Metal Appliqué. *Proceedings of the 17th International Symposium on Ballistics*, Midrand, South Africa, 23–27 March 1998.
29. Taylor, G. I.; The Use of Flat-Ended projectiles for Determining Dynamic Yield Stress. Part I. Theoretical Considerations. *Proc. R. Soc.* **1948**, *194*, 289–299.
30. Maudlin, P. J.; Gray III, G. T.; Cady, C. M.; Kaschner, G. C. High-Rate Material Modelling and Validation using the Taylor Cylinder Impact Test. *Phil. Trans. R. Soc. Lond. A* **1999**, *357*, 1707–1729.
31. Whiffin, A. C. The Use of Flat-Ended projectiles for Determining Dynamic Yield Stress. Part II. Tests on Various Metallic Materials. *Proc. R. Soc.* **1948**, *194*, 300–322.
32. Carrington, W. E.; Gayler, M. L. The Use of Flat-Ended projectiles for Determining Dynamic Yield Stress. Part III. Changes in Microstructure Caused by Deformation Under Impact at High-Striking Velocities. *Proc. R. Soc.* **1948**, *194*, 323–331.
33. Hawkyard, J. B.; Eaton, D.; Johnson, W. The Mean Dynamic Yield Strength of Copper and Low Carbon Steel at Elevated temperatures from Measurements of the ‘Mushrooming’ of Flat-Ended projectiles. *Int. J. Mech. Sci.* **1968**, *10*, 929–948.
34. Wilkins, M. L.; Guinan, M. W. Impact of Cylinders on a Rigid Boundary. *J. Appl. Phys.* **1973**, *44*, 1200–1206.
35. Nichols, A. L., Ed. Users Manual for ALE3D: An Arbitrary Lagrange/Eulerian 2D and 3D Code System; Lawrence Livermore National Laboratory: Livermore, CA, 2009.
36. Gurson, A. L. Continuum Theory of Ductile Rupture by Void Nucleation and Growth. Part I. Yield Criteria and Flow Rules for Porous Ductile Media. *J Engg. Matl. Tech. Trans. ASME* **1977**, *99*, 2–5.
37. Follansbee, P. S.; Kocks, U. F. A Constitutive Description of the Deformation of Copper Based on the use of the Mechanical Threshold Stress as an Internal State Variable. *Acta Metall.* **1988**, *36*, 82–93.
38. Maudlin, P. J.; Davidson, R. F.; Henninger, R. J. *Implementation and Assessment of the Mechanical-Threshold-Stress Model Using the EPIC2 and PINON Computer Codes*; LA-11895-MS; Los Alamos National Laboratory: Los Alamos, NM, 1990.

39. Goto, D. M.; Bingert, J.; Chen, S. R.; Gray, G. T.; Garrett, R. K. The Mechanical Threshold Stress Constitutive Strength Model Description of HY-100 Steel. *Met. and Matls. Trans. A* **2000**, *31A*, 1985–1996.
40. Banerjee, B. The Mechanical Threshold Stress Model for Various Tempers of AISI 4340 Steel. *Int. J. Solids Structs.* **2007**, *44*, 834–859.
41. Regazzoni, G.; Kocks, U. F.; Follansbee, P. S. Dislocation Kinetics at High Strain Rates. *Acta Metall.* **1987**, *35*, 2865–2875.
42. Mecking, H.; Kocks, U. F. Kinetics of Flow and Strain-Hardening. *Acta Metall.* **1981**, *29*, 1865–1875.
43. Tvergaard, V. Material Failure by Void Coalescence in Localized Shear Bands. *Int. J. Solids Structs.* **1982a**, *18*, 659–672.
44. Tvergaard, V. On Localization in Ductile Materials Containing Spherical Voids. *Int. J. Frac.* **1982b**, *18*, 237–252.
45. Tvergaard, V.; Needleman, A. Analysis of the Cup-cone Fracture in a Round Tensile Bar. *Acta Metall.* **1984**, *32*, 157–169.
46. Becker, R. C., Private communications, June-August, 2012.
47. Gray, G. T., Private communications, June 3, 2010.
48. House, J. W.; Lewis, J. C.; Gillis, P. P.; Wilson, L. L. Estimation of Flow Stress Under High Rate Plastic Deformation. *Int. J. Impact Engg.* **1995**, *16*, 189–200.
49. Clayton, J. Modeling Effects of Crystalline Microstructure, Energy Storage Mechanisms, and Residual Volume Changes on Penetration Resistance of Precipitate-Hardened Aluminum Alloys. *Composites, Part B* **2009**, *40*, 443–450.
50. Williams, C. L. *Size-Dependent Strengthening of Particle-Reinforced Aluminum Matrix Composites*; ARL-TR-5530; U.S. Army Research Laboratory: Aberdeen Proving Ground, MD, 2011.

INTENTIONALLY LEFT BLANK.

Appendix. MTS Model Parameters for 6061-T6 Aluminum¹

ALE3D MTS Parameter	Parameter Description	Nominal Value
sig_a	Athermal part of yield stress	50.00 MPa
sig_i	Initial interstitial threshold stress	305.00 MPa
sig_s	Initial solute threshold stress	0.00 MPa
sig_ds	Base saturation value	270.00 MPa
c_const	Hardening rate coefficient, C ₁ , in evolution equation	3800.00 MPa
c_log	Hardening rate coefficient, C ₂ , in evolution equation	0.00 MPa
c_sqrt	Hardening rate coefficient, C ₃ , in evolution equation	0.00 MPa
c_lin	Hardening coefficient, C ₄ , in evolution equation	0.00 MPa
c_pow	Hardening coefficient, C ₅ , in evolution equation	0.00 MPa
c_exp	Hardening coefficient, C ₆ , in evolution equation	0.00 MPa
edot_d	Strain rate, dislocation in hardening law	1.00e4
edot_i	Strain rate, interstitial	1.00e4
edot_s	Strain rate, solute	1.00e4
edot_ds	Strain rate, dislocation in saturation	1.00e4
g0_d	Normalized activation energy, dislocation	1.60
g0_i	Normalized activation energy, interstitial	4.20
g0_s	Normalized activation energy, solute	1.60
g0_ds	Dimensionless activation energy	0.53
qpwr_d	Hardening exponent, dislocation	1.00
qpwr_i	Hardening exponent, interstitial	1.50
qpwr_s	Hardening exponent, solute	1.50
ppwr_d	Hardening exponent, dislocation	0.67
ppwr_i	Hardening exponent, interstitial	0.50
ppwr_s	Hardening exponent, solute	0.50

¹ Becker, R. C., Private communications, June–August, 2012.

List of Symbols, Abbreviations, and Acronyms

ARL	U.S. Army Research Laboratory
IE	internal energy
KE	kinetic energy
L/D	length over diameter
MMC	metal matrix composite
MTS	Mechanical Threshold Stress
SEM	scanning electron microscope

<u>NO. OF COPIES</u>	<u>ORGANIZATION</u>	<u>NO. OF COPIES</u>	<u>ORGANIZATION</u>
1 (PDF only)	DEFENSE TECHNICAL INFORMATION CTR DTIC OCA 8725 JOHN J KINGMAN RD STE 0944 FORT BELVOIR VA 22060-6218	45	ABERDEEN PROVING GROUND DIR USARL RDRL CIH C P CHUNG D GROVE J CAZAMIAS RDRL WM P BAKER B FORCH J MCCUALEY P PLOSTINS RDRL WML J NEWILL M ZOLTOSKI RDRL WML H S SCHRAML RDRL WMM J BEATTY J ZABINSKI RDRL WMM B B CHEESEMAN C-F YEN RDRL WMM D R CARTER RDRL WMM E C HUBBARD RDRL WMP N ELDREDGE S SCHOENFELD RDRL WMP A B RINGERS J BALL RDRL WMP B C HOPPEL S SATAPATHY M LYNCH D POWELL RDRL WMP C T BJORKE R BECKER S BILYK (10 CPS) RDRL WMP D R DONEY RDRL WMP E P SWOBODA E HORWATH T JONES M KORNECKI C KRAUTHAUSER RDRL WMP F N GNIAZDOWSKI R GUPTA RDRL WMP G S KUKUCK
1	DIRECTOR US ARMY RESEARCH LAB IMAL HRA MAIL & RECORDS MGMT 2800 POWDER MILL RD ADELPHI MD 20783-1197		
1	DIRECTOR US ARMY RESEARCH LAB RDRL CIO LL 2800 POWDER MILL RD ADELPHI MD 20783-1197		
1	DIRECTOR US ARMY RESEARCH LAB RDRL CIO LT 2800 POWDER MILL RD ADELPHI MD 20783-1197		
2	LAWRENCE LIVERMORE NATL LAB A ANDERSON D FAUX L-140 PO BOX 808 LIVERMORE CA 94550		

INTENTIONALLY LEFT BLANK.